



**HAL**  
open science

# Accelerating and Stabilizing the Vapor-Liquid Equilibrium (VLE) Calculation in Compositional Simulation of Unconventional Reservoirs Using Deep Learning Based Flash Calculation

Shihao Wang, Nicolas Sobecki, Didier Ding, Lingchen Zhu, Yu-Shu Wu

► **To cite this version:**

Shihao Wang, Nicolas Sobecki, Didier Ding, Lingchen Zhu, Yu-Shu Wu. Accelerating and Stabilizing the Vapor-Liquid Equilibrium (VLE) Calculation in Compositional Simulation of Unconventional Reservoirs Using Deep Learning Based Flash Calculation. *Fuel*, 2019, 253, pp.209-219. 10.1016/j.fuel.2019.05.023 . hal-02142339

**HAL Id: hal-02142339**

**<https://ifp.hal.science/hal-02142339v1>**

Submitted on 28 May 2019

**HAL** is a multi-disciplinary open access archive for the deposit and dissemination of scientific research documents, whether they are published or not. The documents may come from teaching and research institutions in France or abroad, or from public or private research centers.

L'archive ouverte pluridisciplinaire **HAL**, est destinée au dépôt et à la diffusion de documents scientifiques de niveau recherche, publiés ou non, émanant des établissements d'enseignement et de recherche français ou étrangers, des laboratoires publics ou privés.

# Accelerating and Stabilizing the Vapor-Liquid Equilibrium (VLE) Calculation in Compositional Simulation of Unconventional Reservoirs Using Deep Learning Based Flash Calculation

Shihao Wang<sup>1</sup>, Nicolas Sobecki<sup>2</sup>, Didier Ding<sup>2</sup>, Lingchen Zhu<sup>3</sup>, Yu-Shu Wu<sup>1</sup>

<sup>1</sup>*Petroleum Engineering Department, Colorado School of Mines, Golden, CO 80401, USA*

<sup>2</sup>*IFPEN, France*

<sup>3</sup>*Schlumberger Doll Research Center, Cambridge, MA 02139, USA*

## Abstract

The flash calculation with large capillary pressure often turns out to be time-consuming and unstable. Consequently, the compositional simulation of unconventional oil/gas reservoirs, where large capillary pressure exists on the vapor-liquid phase interface due to the narrow pore channel, becomes a challenge to traditional reservoir simulation techniques. In this work, we try to resolve this issue by combining deep learning technology with reservoir simulation. We have developed a compositional simulator that is accelerated and stabilized by stochastically-trained proxy flash calculation.

We first randomly generated 300,000 data samples from a standalone physical flash calculator. We have constructed a two-step neural network, in which the first step is to classify the phase condition of the system and the second step is to predict the concentration distribution among the determined phases. Each network consists of four hidden layers in between the input layer and the output layer. The network is trained by Stochastic Gradient Descent (SGD) method with 100 epochs.

With given temperature, pressure, feed concentration pore radius, the trained network predicts the phases and concentration distribution in the system with very low computational cost. Our results show that the accuracy of the network is above 97% in the metric of mean absolute percentage error. The predicted result is used as the initial guess of the flash calculation module in the reservoir simulator. With the implementation of the deep learning based flash calculation module, the speed of the simulator has been effectively increased and the stability (in the manner of the ratio of convergence) has been improved as well.

## Keywords

Flash calculation; unconventional reservoirs; deep learning; proxy calculation; reservoir simulation

## 1. Introduction

The oil and gas stored in unconventional reservoirs has some unique transport mechanism and phase behavior, including the pore confine effect [1,2], the large capillary pressure effect [3,4], multiscale pore structures [5] and gas slippage effect [6–9]. Moreover, the prediction of the complex

36 phase behaviors in unconventional reservoirs requires compositional modeling, of which the flash  
37 calculation is an essential yet time-consuming portion. To improve the speed as well as the stability of  
38 the flash calculation, several techniques have been adopted, including reduction method [10], phase  
39 stability test [11] and so on. Recently, the fast-arising artificial intelligence (AI) techniques have drawn  
40 the attention of researchers. Particularly, the fast development of the optimization algorithm, as well as  
41 hardware infrastructure, have greatly promoted the advance of stochastic learning techniques. The  
42 rapid development of GPU enables the training of deep learning (DL) networks (also known as Artificial  
43 Neural Network (ANN)) [12]. There are several trials of combining AI with flash calculation. Gaganis et  
44 al. [13,14] are among the first to propose the application of neural network approach in developing  
45 proxy flash calculation. In their work, support vector classifier (SVC) is used to conduct phase stability  
46 test and a single layer ANN network is used to replace the physical flash calculation for liquid-vapor  
47 phase equilibrium calculation. Kashinath et al. [15] further improved Gaganis et al.'s model by bringing  
48 out a novel framework to conduct an isothermal flash calculation. In their work, the relevance vector  
49 machine [16] is combined with an single-layer artificial neural network. The former technique is used to  
50 classify phase condition, while the latter is used to determine the concentration distribution. All these  
51 proxy models have shown sound accuracy and have been successfully implemented into reservoir  
52 simulators, improving the speed of compositional simulation. Moreover, El-Sebakhy [17] and Rafiee-  
53 Taghanaki et al. [18] used the support vector machine technique [19–22] to predict the PVT properties  
54 of crude oil, including gas oil ratio, oil volume factor, density and so on. Artificial neural networks have  
55 also been used to predict the PVT behavior of crude oil [23] and gas mixtures [24]. Nikravesht et al. [25]  
56 reviewed the applications of artificial intelligence techniques in the exploration and development of  
57 petroleum reservoirs.

58 In this work, we further extend the work listed above to the compositional simulation of  
59 unconventional reservoirs with large capillary pressure effect. We have developed a deep-learning  
60 based flash calculation module (proxy flash calculation) for the prediction of phase behaviors of oil and  
61 gas in unconventional reservoirs. This proxy flash calculation adopts multi-layer fully connected layers  
62 to regress the training data. The input parameters of our model include pressure, temperature, feed  
63 concentration and pore radius. The accuracy of the network is above 97% in the metric of mean  
64 absolute percentage error. The proxy flash calculation module is used as a preconditioner of the  
65 physical flash calculation and has been implemented in a reservoir simulator. We have also compared  
66 the performance of the network with different number of hidden layers. The novelty of this work lies in  
67 the implementation of the deep learning based flash calculation module as a preconditioner for both  
68 phase condition detection and concentration determination, which improves the speed as well as the  
69 stability of compositional simulation of unconventional reservoirs while maintaining the same results as  
70 physical flash calculation.

This paper is organized as follows. In Chapter 2, we present the physical flash calculation used to train the network. In Chapter 3, we describe the structure, training as well as results of our deep-learning based flash calculation module. In Chapter 4, we describe the implementation of the developed module into an in-house reservoir simulator. In Chapter 5, we present the results of field scale reservoir simulation. In Chapter 6, we summarize and conclude this work.

## 2. Forward modeling

In this section, we briefly introduce the governing equations and flash calculation module used for the forward modeling.

### 2.1. Flow governing equations

The reservoir simulator used in this work is named as MSFLOW\_CO2 [3,26,27]. MSFLOW\_CO2 is a general three-dimensional reservoir simulator for the simulation of complex multiphase flow in porous media. Based on the law of mass conservation, the flow governing equations of MSFLOW\_CO2 describe the transport of hydrocarbon components in a petroleum reservoir. For a vapor-liquid compositional system with  $N_C$  components, the mass conservation equation for component  $k$  is as below

$$\frac{\partial}{\partial t} \left( \phi \sum_{\beta} S_{\beta} \rho_{\beta} x_{\beta}^k \right) = \nabla \cdot \left[ -K_a \frac{K_{r\beta} \rho_{\beta}}{\mu_{\beta}} (\nabla P_{\beta} - \rho_{\beta} \vec{g}) x_{\beta}^k \right] + q^k, \quad \beta = L, G, \quad k = 1, \dots, N_C \quad 1$$

where  $\phi$  is the rock porosity.  $\beta$  is the phase index referring to the liquid (L) or vapor/gas (G) phase.  $S_{\beta}$  and  $\rho_{\beta}$  are the saturation and density of phase  $\beta$ , respectively.  $K_{r\beta}$ ,  $\mu_{\beta}$  and  $P_{\beta}$  are the relative permeability, viscosity and pressure of phase  $\beta$ , respectively.  $K_a$  is the apparent permeability. While for the liquid phase,  $K_a$  is the same as the rock absolute permeability  $K_{\infty}$ , for the vapor phase,  $K_a = K_{\infty}(1+b/p)$ , in which  $b$  is the Klinkenberg parameter.  $x_{\beta}^k$  is the mole concentration of component  $k$  in phase  $\beta$ .  $\vec{g}$  is the gravity term and  $q$  is the sink/source term. In this work the pore compressibility is temporally ignored.

In MSFLOW\_CO2, Equation 1 is discretized and solved by the Integrated Finite Difference (IFD) method, the details of which can be found in Ref. [28]. The flow between the rock matrix and the fracture system is described by the dual-porosity model [29]. The nonlinear system resulted from the discretization of IFD is solved by Newton-Raphson's approach. Within each nonlinear iteration, the resulted linear system is solved by a multiscale linear solver [30].

## 2.2. Flash calculation with capillary pressure

In a compositional reservoir simulator, given the pressure ( $P$ ), temperature ( $T$ ) and mole concentration of each component ( $z_i$ ), the flash calculation module predicts the phase condition as well as the concentration of each component in each phase.

In this work, we consider a two-phase system with vapor ( $V$ ) and liquid ( $L$ ) phase. The mole concentration of a component in the vapor (gas) phase and in the oil (liquid) phase is denoted respectively as  $y_i$  and  $x_i$ . Meanwhile, the total mole concentration of the vapor phase and the oil phase is denoted as  $n_V$  and  $n_L$  respectively. We then have the following relationship.

$$z_i = x_i n_L + y_i n_V \quad 2$$

The phase behavior of fluids stored in unconventional reservoirs is unlike that in conventional reservoirs. In the narrow pores of unconventional reservoirs, the capillary pressure  $P_c$  between phases can be no longer ignored [31,32]. For simplicity, in this work, the capillary pressure, which is the difference between the vapor pressure  $p^V$  and the oil phase pressure  $p^L$ , is calculated as below, assuming the oil phase is the wetting phase.

$$P_c = p^V - p^L = \frac{2\sigma_{VL}\cos\theta}{r} \quad 3$$

In the above equation,  $\sigma_{VL}$  is the interfacial tension between the vapor phase and the liquid phase.  $\theta$  is the contact angle and  $r$  is the pore radius.

$\sigma_{VL}$  is calculated using the model from the work of Macleod [33] and Sugden [34], as follows

$$\sigma_{VL} = \left( P_a^L \rho^L - P_a^V \rho^V \right)^\nu = \left( \rho^L \sum_{i=1}^{N_C} x_i P_{a,i} - \rho^V \sum_{i=1}^{N_C} y_i P_{a,i} \right)^\nu \quad 4$$

where  $\rho^L$  and  $\rho^V$  is the molar density of the liquid phase and the vapor phase respectively.  $P_a^L$  and  $P_a^V$  is the parachor for the liquid phase and the vapor phase respectively.  $P_{a,i}$  is the parachor of component  $i$ , the value of which is listed in Table A.2.  $\nu$  is a parameter that is by default set to be 3.6 [35].

At the equilibrium condition, the fugacity of component  $i$  in the vapor phase  $f_i^V$  and in the liquid phase  $f_i^L$  should be equal, as

$$f_i^V = f_i^L \quad 5$$

We introduce the fugacity coefficient of component  $i$  in the vapor phase and the liquid phase, as

$$126 \quad \Phi_i^V = \frac{f_i^V}{y_i P^V} \quad 6$$

$$127 \quad \Phi_i^L = \frac{f_i^L}{x_i P^L} \quad 7$$

128 Moreover, the equilibrium ratio is defined as

$$129 \quad K_i = \frac{y_i}{x_i} = \frac{f_i^V / (\Phi_i^V P^V)}{f_i^L / (\Phi_i^L P^L)} = \frac{\Phi_i^L P^L}{\Phi_i^V (P^L + P_c)} \quad 8$$

130 By combining Equation 5 and Equation 8 and considering the constraints that  $\sum_{i=1}^{N_c} z_i = \sum_{i=1}^{N_c} y_i = \sum_{i=1}^{N_c} x_i = 1$ ,

131 we can derive the Rachford-Rice equation as

$$132 \quad \sum_{i=1}^{N_c} \frac{z_i (K_i - 1)}{n_L + K_i (1 - n_L)} = 0 \quad 9$$

133 In this work, Peng-Robin equation of state (PR-EOS) [36] without volume factor correction is used for  
134 the calculation of the PVT properties of oil and gas. PR-EOS is a widely adopted cubic equation of  
135 state. For phase  $\beta$  (vapor or liquid), the compressibility can be formulated as

$$136 \quad (Z^\beta)^3 + (B^\beta - 1)(Z^\beta)^2 + (A^\beta - 3(B^\beta)^2 - 2B^\beta)Z^\beta - (A^\beta B^\beta - (B^\beta)^2 - (B^\beta)^3) = 0, \dots, \beta = L, V \quad 10$$

137 where the term  $A^\beta$  and  $B^\beta$  are defined as follows

$$138 \quad A^\beta = \frac{a_m P^\beta}{R^2 T^2} \quad 11$$

$$139 \quad B^\beta = \frac{b_m P^\beta}{RT}$$

140 12

141 In the above equations,  $Z^\beta$  is the compressibility of phase  $\beta$ . the terms  $a_m$  and  $b_m$  are defined as

142 follows as

$$143 \quad a_m = \sum_{i=1}^{N_c} \sum_{j=1}^{N_c} z_i z_j a_{ij} \quad 13$$

$$144 \quad a_{ij} = (1 - k_{ij}) \sqrt{\alpha_i a_i \alpha_j a_j} \quad 14$$

$$145 \quad a_i = 0.45724 \frac{R^2 T_{c_i}^2}{P_{c_i}} \quad 15$$

148

$$149 \quad \alpha_i = \left[ 1 + S_i^* \left( 1 - \sqrt{T_{c_i}/T} \right) \right]^2 \quad 16$$

$$150 \quad S_i^* = 0.37464 + 1.54226\omega_i - 0.26992\omega_i^2 \quad 17$$

$$151 \quad b_m = \sum_{i=1}^{N_c} b_i \quad 18$$

$$152 \quad b_i = 0.0778 \frac{RT_{c_i}}{P_{c_i}} \quad 19$$

153 where  $R$  is the gas constant.  $\omega$  is the acentric factor.  $k_{ij}$  is the binary interaction coefficient between  
 154 component  $i$  and the component  $j$ .  $T_c$  and  $P_c$  is the critical temperature and critical pressure  
 155 respectively. The critical properties for the hydrocarbon used in this work are from NIST data [37]. The  
 156 largest root of the cubic equation is assigned to the compressibility of the vapor phase, while the  
 157 smallest root is assigned to the compressibility of the liquid phase. Based on the assumption of  
 158 isothermal flash calculation, in PR-EOS, the fugacity coefficients are calculated as

$$159 \quad \ln(\Phi_i^\beta) = \frac{b_i(Z^\beta - 1)}{b_m} - \ln(Z^\beta - B^\beta) - \frac{A^\beta}{2\sqrt{2}B^\beta} \left( \frac{2\Psi_i}{a_m} - \frac{b_i}{b_m} \right) \ln \left( \frac{Z^\beta + (1 + \sqrt{2})B^\beta}{Z^\beta - (1 - \sqrt{2})B^\beta} \right) \quad 20$$

160 In the above equation, the term  $\Psi_i$  is

$$161 \quad \Psi_i = \sum_j x_j \sqrt{a_i a_j \alpha_i \alpha_j} (1 - k_{ij}) \quad 21$$

162 The initial guess of the equilibrium ratio  $K_i^0$  is calculated by Wilson's equation

$$163 \quad K_i^0 = \frac{P_{c_i}}{p} \exp \left( 5.37(1 + \omega_i) \left( 1 - \frac{T_{c_i}}{T} \right) \right) \quad 22$$

164 Initially, the capillary pressure is set to be 0.

165 Prior to the flash calculation, a Gibbs energy based phase stability test is performed to  
 166 preliminarily determine the single phase region. The approach used here follows the work of Sherafati  
 167 and Jessen [35]. The tangent plane distance (TPD) based on Michelsen's formulation [38] is as follows

$$168 \quad TPD(\mathbf{z}_T) = \sum_{i=1}^{N_c} z_{T_i} \left[ \mu_i^T(\mathbf{z}_T, P^T) - \mu_i^z(\mathbf{z}, P^z) \right] \quad 23$$

169 where  $\mathbf{z}$  and  $\mathbf{z}_T$  refers to the mole concentration of the feed and a trial phase, respectively.  $\mu_i^T$  and  $\mu_i^z$  is  
 170 the fugacity of component  $i$  in the trial phase and the feed respectively.  $P^T$  and  $P^z$  is the trial phase  
 171 pressure and the reference pressure respectively. By switching the variable  $\ln Z_i^T = \ln z_i^T - k$  where  $k$  is  
 172 the reduced value of the tangent plane distance at the stationary points of Equation 23, the above  
 173 equation can be expressed as

$$174 \quad TPD(\mathbf{Z}_T) = 1 + \sum_{i=1}^{N_c} Z_{Ti} \left[ \ln Z_{Ti} + \ln \phi_i^T + \ln P^T - (\ln z_i + \ln \phi_i + \ln P^z) - 1 \right] \quad 24$$

175 where  $\phi_i$  and  $\phi_i^T$  denotes the fugacity coefficient of component  $i$  in the feed and the trial phase,  
 176 respectively. Finding the stationary points of TPD is equivalent to solving the below equation

$$177 \quad \ln Z_{Ti} + \ln \phi_i^T + \ln P^T - (\ln z_i + \ln \phi_i + \ln P^z) = 0 \quad 25$$

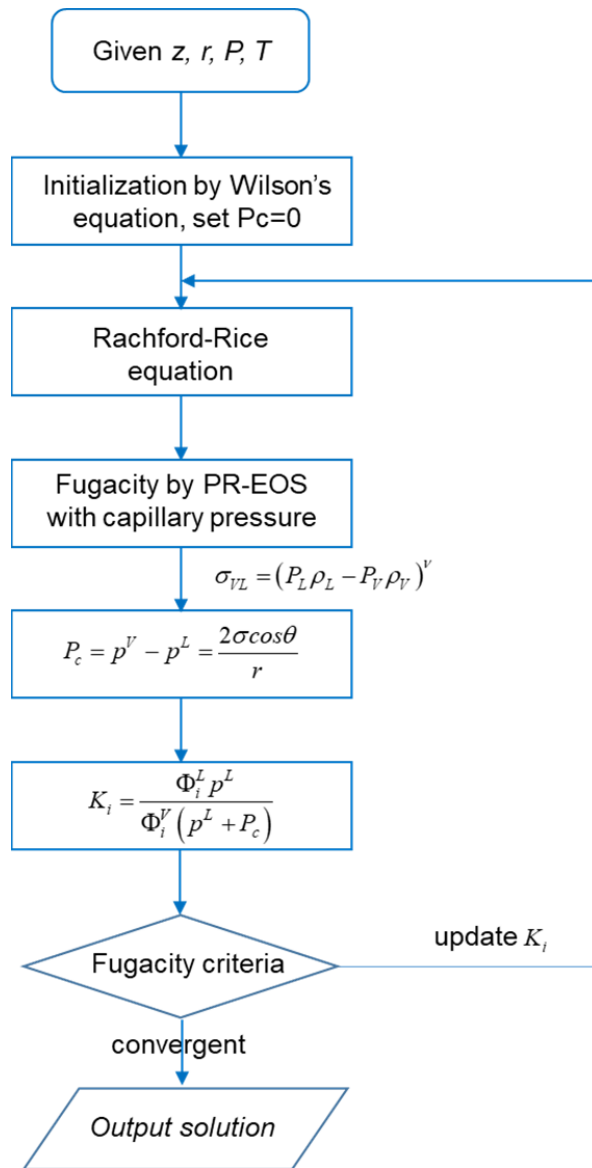
178 The above equation is iteratively solved by an accelerated direct substitution approach based on  
 179 dominant eigenvalue method, as described by Orbach and Crowe [39]. It should be noticed that, unlike  
 180 the phase stability test without capillary pressure, the solution of Equation 25 should take the pressure  
 181 difference between the trial phase and the feed into consideration, as  $P^T - P^z = \pm P_C$ . The sign before  
 182 the capillary pressure is positive if the trial phase is the non-wetting (vapor) phase and the feed is the  
 183 wetting (liquid) phase. The sign is negative if the trial phase and the feed is wetting phase and non-  
 184 wetting phase respectively.

185 Based on the solution of the Rachford-Rich equation and the capillary pressure equation, the  
 186 fugacities, as well as densities of the fluids, are obtained. The algorithm iteratively tunes the solution to  
 187 minimize the residual of the equilibrium ratio as well as the capillary pressure until certain criteria are  
 188 satisfied. In this work, the criterion of the convergence of the equilibrium ratio is set as

$$189 \quad \sum_i \left| \frac{K_i}{K_i^*} - 1 \right| \leq 1.0e^{-4} \quad 26$$

190 where  $K_i^*$  is the equilibrium ratio solved at the previous iteration step. A flowchart of the K-value based  
 191 flash calculation with capillary pressure effect is shown in Figure 1. The parameters, including binary  
 192 interaction factor and parachor values, for the physical flash calculation are listed in Appendix A. As an  
 193 example, the phase envelopes of n-Decane-CO<sub>2</sub> binary mixture with and without the capillary pressure  
 194 are shown in Figure 2. Our results match well with experimental results [40].  
 195





196

197

**Figure 1** Flowchart of the K-value based flash calculation with capillary pressure effect.

198

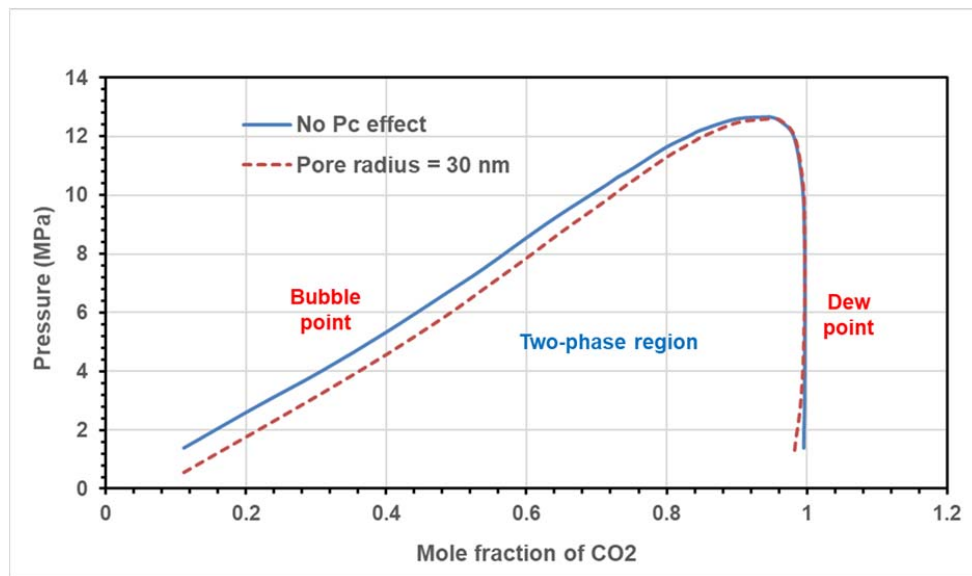


Figure 2 Phase envelop of n-Decane-CO<sub>2</sub> binary mixture at 71 °C.

199  
200

201  
202

### 203 3. Proxy flash calculator

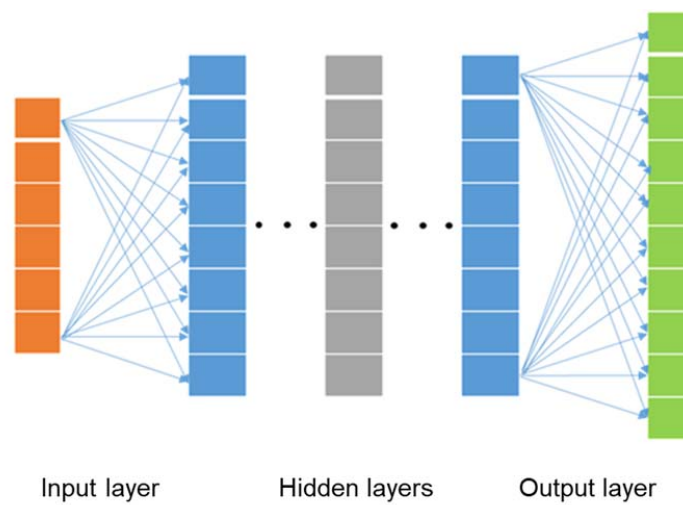
#### 204 3.1. General information

205 In this work, we have developed a data-driven flash calculation module based on deep learning  
 206 techniques to improve the speed and convergence performance of the flash calculation in the  
 207 unconventional reservoirs. In the new framework, the initial guess of the flash calculation is obtained  
 208 from a stochastically trained neural network instead of Wilson's equation. We use deep-learning based  
 209 stochastic training technique to develop the proxy simulator. We have trained a neural network, which  
 210 has an input layer, an output layer, and four hidden layers. Within each layer, there are several neurons  
 211 (elements). All neurons belonged to two neighboring layers are fully connected, as shown in Figure 3.

212 The neural network adopts fully connected (dense) layers and is trained as a standalone  
 213 module. Once trained, the neural network predicts the phase condition, capillary pressure as well as  
 214 concentration distribution by simple interpolations. As will be shown in the later chapters, the accuracy  
 215 of the developed network is above 97%. Therefore, a much more accurate initial guess for the flash  
 216 calculation can be obtained. The fully connected layers are an imitation of human's neural system.  
 217 Each element within the network has one weight value and one bias value, indicating the 'contribution'  
 218 of the element. In the fully connected layers, each element is connected to all elements belonged to its  
 219 neighboring layers. Activation functions are used between layers. For a given set of input parameters,  
 220 the network predicts the output results by interpolating from the weight values and the bias values.  
 221 During the training process, the weight and the bias of the elements are optimized by certain  
 222 optimization algorithms to achieve the best prediction. Then in the prediction step as shown in Figure 4,

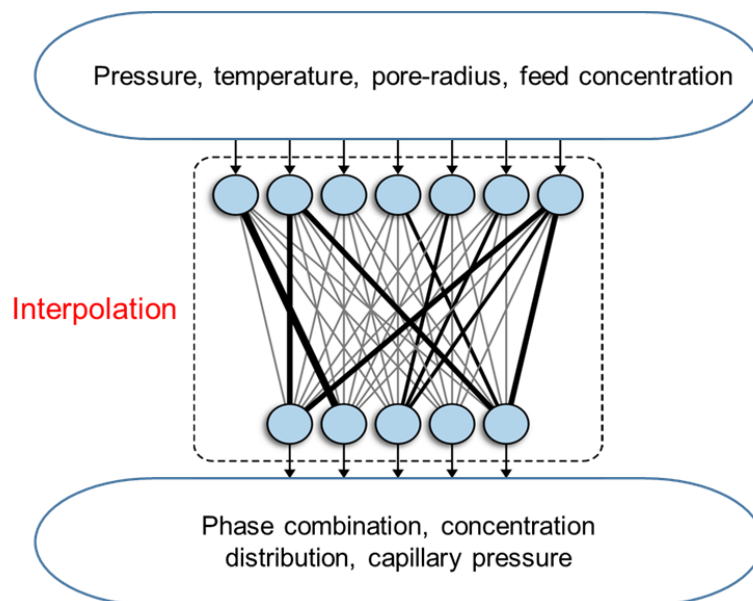
223 the simulator only needs to load the trained weight and bias values into the memory and conduct  
 224 simple interpolation, which is very cheap in terms of computational time.

225 In this work, the training process consists of two steps. The first step, which is named the phase  
 226 classification step, determines the phase condition of the system under the given condition. In the  
 227 second step, which is named the concentration determination step, the phase ratio, component  
 228 concentration, and capillary pressure are determined. The input parameters for both steps include  
 229 pressure, temperature, feed concentration and pore radius. The input parameters are all normalized to  
 230  $[0,1]$  scale before being substituted into the network.



231  
 232

**Figure 3 Conceptual model of the fully connected neural network.**



233  
 234  
 235

**Figure 4 Conceptual framework of the prediction step.**

### 236 3.2. Phase classification

237 The network for the phase classification step consists of six layers, including the input layer  
 238 (layer 1), the output layer (layer 6) and four hidden layers (layer 2 to 5). The number of input  
 239 parameters is  $N_c + 3$ . The input parameters  $x$  include the feed concentration, pressure, temperature,  
 240 and pore radius. All input parameters are normalized to  $[0,1]$  scale. The dimension of layer 1 to layer 4  
 241 is 64, and the dimension of the output layer is 3. Therefore, the network classifies the phase condition  
 242 into three types, namely pure vapor phase (V), pure oil phase (L), and double phases (V+L).

$$243 \quad X = [P, T, r, z_1, \dots, z_{N_c}]^T \quad 27$$

244 The activation function for layer 1 to 4 is ReLU function, as follows

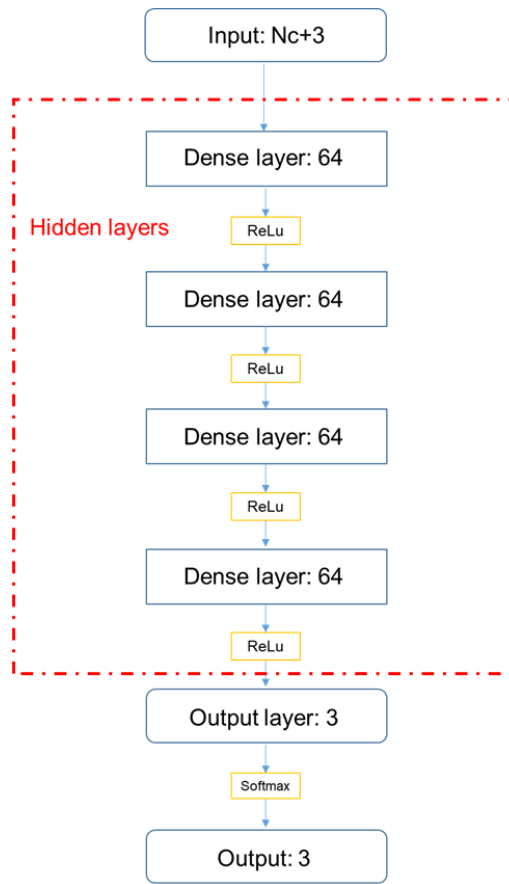
$$245 \quad \text{ReLU}(x) = \begin{cases} 0 & \text{for } x < 0 \\ x & \text{for } x \geq 0 \end{cases} \quad 28$$

246 The activation function for the output layer is Softmax function, as follows

$$247 \quad \text{softmax}(x)_j = \frac{e^{x_j}}{\sum_{k=1}^K e^{x_k}} \quad 29$$

248 where  $K$  is the total number of parameters and  $e^x$  is the exponential function. A detailed structure of the  
 249 network is as shown in Figure 5.

250



251

252

253

**Figure 5 Structure of the fully connected neural network for the phase classification step. The numbers refer to the dimension of the layers.**

254

### 255 3.3. Concentration determination

256

257

258

259

260

261

262

263

The network for the concentration determination step consists of six layers, including the input layer (layer 1), the output layer (layer 6) and four hidden layers (layer 2 to 5). The dimension, as well as physical meanings of the input parameters of this step, are the same as those of the phase classification step. The dimension of layer 1 to layer 4 is 64, and the dimension of the output layer is  $2N_c + 3$ , including the capillary pressure  $P_C$ , the vapor phase ratio  $n_V$ , the oil phase ratio  $n_L$ , and the component concentration in the vapor phase  $y_i, i = 1, \dots, N_c$  and oil phase  $x_i, i = 1, \dots, N_c$ . The activation function for layer 1 to 4 is ReLU function, as shown in Equation 28. The activation function for the output layer is Sigmoid equation, as shown in Equation 30.

264

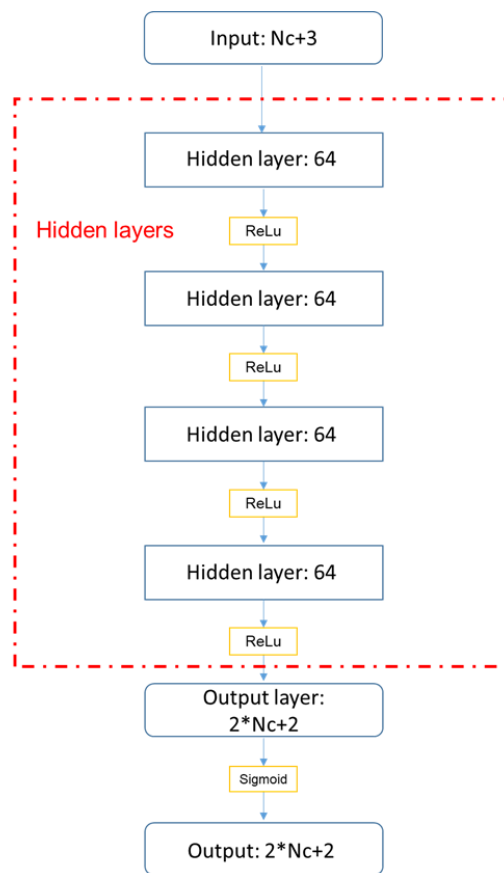
$$\text{sigmoid}(x) = \frac{1}{1 + e^{-x}}$$

30

265

A detailed structure of the network is as shown in Figure 6.

266



267

268 **Figure 6 Structure of the neural network for the concentration determination step. The numbers**  
 269 **refer to the dimension of the layers.**

270

### 271 3.4. Training

272 We have investigated five cases with different combinations of hydrocarbon components. For  
 273 each case, we use 300,000 training samples generated from the standalone flash calculation module  
 274 described in Chapter 2. The samples are generated randomly using Latin Hypercube Sampling [41,42]  
 275 technique. The range of the input parameters is listed in Table 1.

276

277

Table 1 Range of the parameters of the training samples.

	Unit	Minimum	Maximum
Pressure	MPa	1	80
Temperature	°C	40	100
Pore radius	nm	30	100
Feed concentration	dimensionless	0	1

278

279

280 We use stochastic gradient descent (SGD) algorithm [43] to train the network on Keras [44] with a GTX  
 281 1080Ti GPU of 11 GB in memory. The algorithm of SGD can be briefly described as follows (Bottou  
 282 2012). For an object function  $Q$  with the primary variable  $\mathbf{w}$  of  $n$  dimensions,

$$283 \quad \Theta(\mathbf{w}) = \frac{1}{n} \sum_{i=1}^n \Theta_i(w_i) \quad 31$$

284 Instead of optimizing all  $n$  dimensions at the same time, SGD randomly optimizes a randomly chosen  
 285 group (batch) of the variables using gradient descent optimization, as below

$$286 \quad w_{t+1} = w_t - \eta \nabla_j \Theta(w_t) \quad 32$$

287 where  $t$  is the number of iteration steps.  $j$  is the index of a batch.  $\eta$  is the learning rate. After the  
 288 completion of one epoch, all the training samples are shuffled. Hence, the optimization of one high-  
 289 dimensional problem is effectively converted to the optimization of numerous low-dimensional  
 290 problems. In this work, we have compared the choice of the learning rate. The optimal value is found to  
 291 be 0.001. The neural network for the phase classification step and the concentration determination step  
 292 is trained with 100 epochs, respectively. We use the mean absolute percentage error (MAPE) as a  
 293 metric (loss function) during the training, which is defined as follows.

$$294 \quad \text{MAPE} = \frac{100\%}{N} \sum_{i=1}^N \left| \frac{A_i - F_i}{A_i} \right| \quad 33$$

295 In the above equation,  $N$  refers to the number of testing samples.  $A$  and  $F$  refer to actual value and  
 296 predicted (forecast) value, respectively. The accuracy of the training sample is cross validated by K-  
 297 folds approach. The training samples are randomly divided into ten groups. For every ten epochs of the  
 298 training, one group is chosen for testing and the rest of the nine groups are used for training. The  
 299 variation of the loss function during the training process for Case 5 is shown in Figure 7. The error  
 300 metric for each of the five cases is listed in Table 2. According to the results, the accuracy of our neural  
 301 network is above 97% for the cases we run. We have compared the accuracy of the network with  
 302 different number of hidden layers and found out network with four hidden layers achieves optimal  
 303 performance. Generally speaking, more hidden layers (with more degree of freedom) result in deeper  
 304 network and better accuracy. However, beyond a certain level the addition of more layers cannot  
 305 contribute to accuracy and may even cause over-fitting issue [12]. We have also compared the  
 306 performance of different activation functions for the hidden layers, including sigmoid function (as  
 307 defined in Equation 30), tanh function [12] and ReLU function (as defined in Equation 28) for Case 4.  
 308 The results are listed in Figure 9, which shows that ReLU function achieves the highest accuracy.  
 309 However till today the choice of activation function as well as the number of layers is still like an art.  
 310 Moreover, as expected when the number of hydrocarbon components increases, the accuracy  
 311 decreases accordingly, due to the increase of the dimensions in the parameter space. In general, the  
 312 proxy flash calculator based on deep learning techniques is much more accurate than any other

313 existing techniques.

314

315

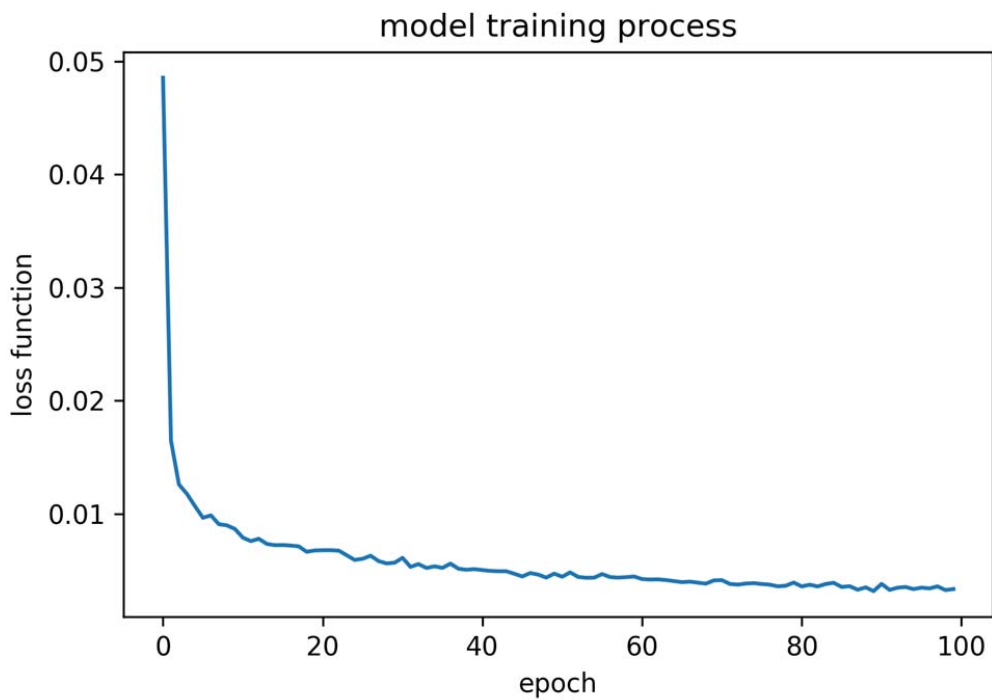
316

**Table 2 Summary of errors of the fully connected network.**

Case index	Feed component	Phase Classification	Concentration Determination	Overall Accuracy
		Mean Absolute Percentage Error	Mean Absolute Percentage Error	Mean Absolute Percentage Accuracy
1	C1+C2+C3	0.01%	0.46%	99.53%
2	C1+C2+C3+C6	0.02%	0.73%	99.25%
3	C1+C2+C3+C4+C5	0.02%	1.02%	98.96%
4	C1+C2+C3+C5+C7+C9	0.04%	1.86%	98.10%
5	C1+C2+C3+C4+C5 C8+C9+C10	0.06%	2.24%	97.83%

317

318



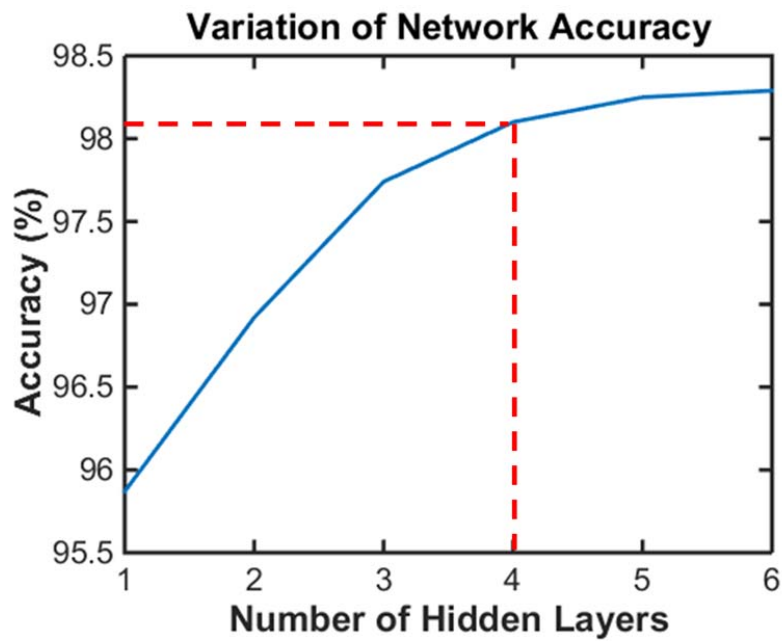
319

320

321

**Figure 7 Variation of the loss function of the phase classification step during the training process of Case 4.**



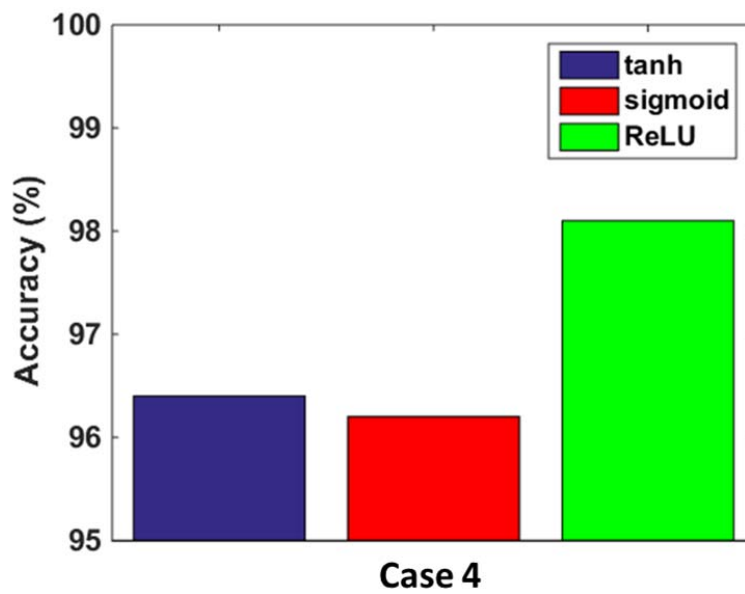


322

323

Figure 8 Comparison of the accuracy with different number of hidden layers for Case 4.

324



325

326

Figure 9 Comparison of the performance of different activation functions for the hidden layers in Case 4.

327

328

329

---

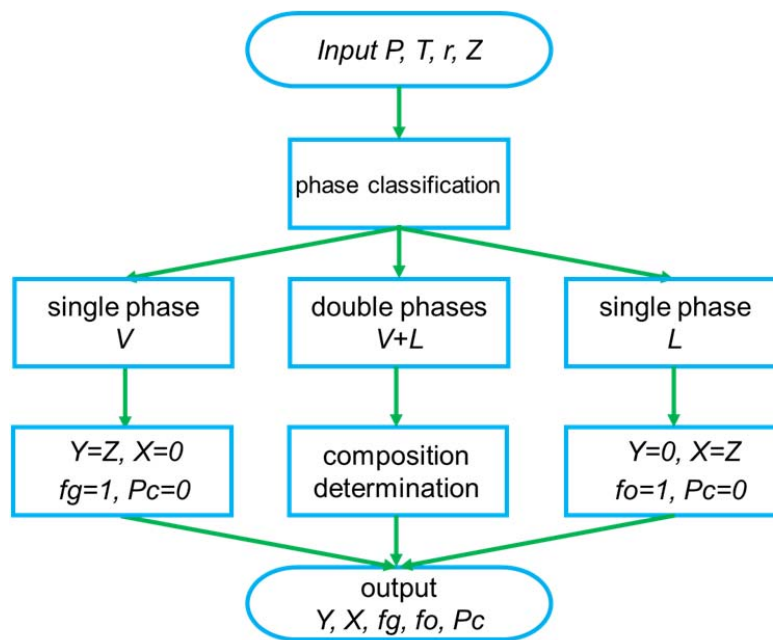
#### 330 4. Deep learning based flash calculator

331 The trained deep learning (DL) network is implemented in our flash calculation module. The  
332 proxy flash calculator provides the initial guess of the equilibrium ratio as well as the capillary pressure,  
333 replacing Wilson's equation. Since the phase classification step is of very high accuracy, the phase  
334 condition predicted by that step is adopted as the 'final' result. Therefore, if the phase classification step  
335 predicts that only one phase exists in the system, the DL proxy calculator directly outputs the results. If,  
336 however, the phase classification step predicts that two phases exist in the system, the flash calculator  
337 will start the K-value based iteration using the predicted equilibrium ratio and capillary pressure, until  
338 global convergence. A simplified and a detailed flowchart of the deep learning based flash calculator  
339 are shown in Figure 10 and Figure 11 respectively.

340 The comparison between the average number of iterations of the flash calculation with and  
341 without DL preconditioning is shown in Table 3. According to the comparison of the numerical  
342 performance, the number of iterations has been cut by above 50%. According to the results, DL based  
343 proxy calculation effectively reduces the number of iterations of flash calculation and, thus accelerates  
344 the reservoir simulation.

345 Moreover, we have observed that DL based preconditioner effectively improves the stability  
346 (convergence) of flash calculation. The large capillary effect causes the flash calculation with Wilson's  
347 initial guess to be difficult to get converged, which prohibits its applications. As shown in Table 4, with  
348 the implementation of the DL based preconditioner, the ratio of the converged flash calculations among  
349 the 300,000 data sets (parameters shown in Table 1) increases from 90% to above 98%. This is also  
350 because that the DL based preconditioner provides a much more accurate initial guess to the flash  
351 calculation, making it close enough to the real solution for the Newton-based algorithm to converge.

352



353

354

Figure 10 Flowchart of the proxy flash calculation in a reservoir simulator.

355

356

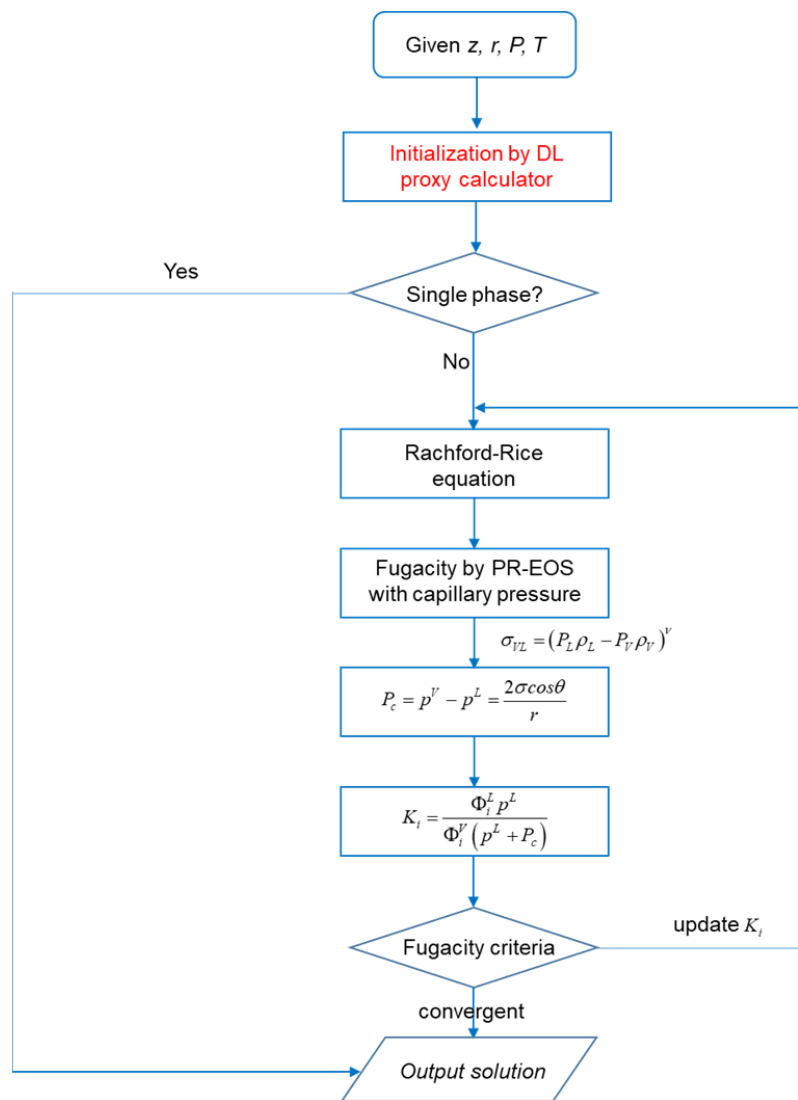


Figure 11 Flowchart of the deep leaning based flash calculator.

357  
358

359  
360  
361  
362  
363  
364  
365  
366

Table 3 Comparison of the number of iterations with and without the number of deep-learning based preconditioner.

Case index	Feed component	Iterations without DL preconditioner	Iterations with DL preconditioner
1	C1+C2+C3	3.7	1.3
2	C1+C2+C3+C6	8.6	2.0
3	C1+C2+C3+C4+C5	14.3	2.2

4	C1+C2+C3+C5+C7+C9	17.0	3.6
5	C1+C2+C3+C4+C5 C8+C9+C10	25.8	4.5

367

368

369

370

**Table 4 Comparison of the ratio of convergence with and without the number of deep-learning based preconditioner.**

Case index	Feed component	Ratio of convergence without DL preconditioner	Ratio of convergence with DL preconditioner
1	C1+C2+C3	96.1%	99.4%
2	C1+C2+C3+C6	94.9%	99.1%
3	C1+C2+C3+C4+C5	93.4%	98.8%
4	C1+C2+C3+C5+C7+C9	92.7%	98.5%
5	C1+C2+C3+C4+C5 C8+C9+C10	91.3%	98.3%

371

372

373

## 5. Case study

374

375

376

377

378

379

380

381

We have implemented the deep-learning based flash calculator into our simulator MSFLOW\_CO2 and have conducted several case studies to investigate the performance of the deep learning based compositional simulator. In this chapter, all numerical cases are executed by an Intel i7-6700 processor with 3.40 GHz. We have investigated the compositional simulation of a fractured reservoir. The reservoir is naturally fractured. A horizontal well is drilled through the reservoir, and a hydraulic fracture is engineered within the reservoir, creating a stimulated reservoir volume (SRV) in the vicinity of the hydraulic fracture. The conceptual model of the problem is shown in Figure 12, in which the green and the orange part indicates the area within and outside the SRV, respectively.

382

383

384

385

386

387

388

389

390

The natural fractured reservoir part and the SRV are both modeled as dual-porosity systems. In the dual-porosity system, the fracture network provides flow channel while the matrix rock stores the hydrocarbon. A 'shape-factor' [46–48] is used to quantify the flow between the matrix rock and the fracture network. Wu and Pruess [49] incorporated the shape factor into the integrated finite difference (IFD) framework. Therefore, in this work the single-continuum and dual-porosity model are both discretized using the same IFD approach, as suggested by Wu and Qin [50]. The length of the entire reservoir along x- and y- direction is 540m and the 400m, respectively, while the length of the SRV along x- and y-direction is 120m and 160m, respectively. The conceptual model of the case is shown in Figure 12. The relative permeability of the gas phase and the oil phase is modeled by the classic

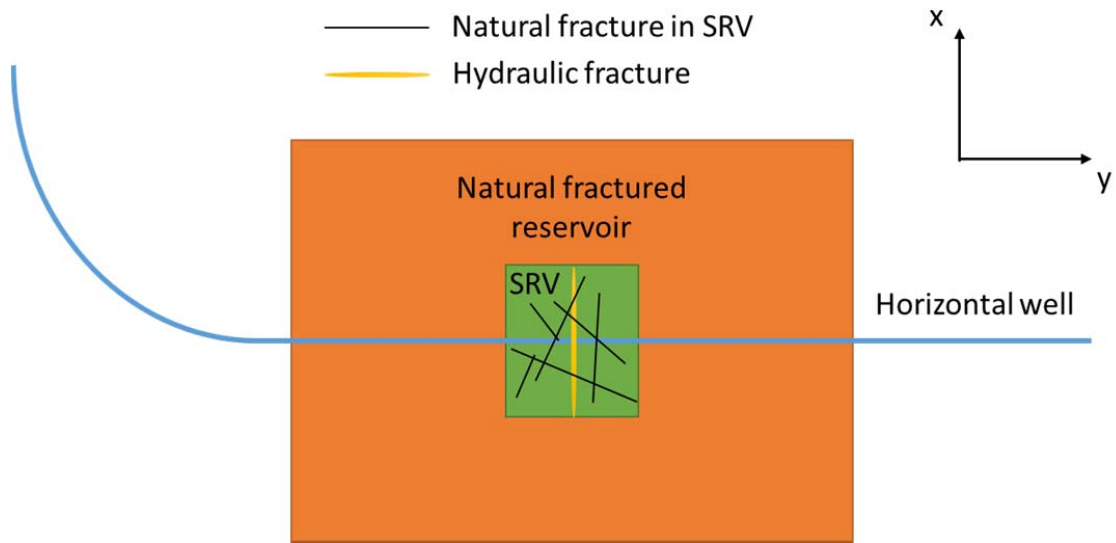
391 Brooks-Corey model [51], as shown in Equation 34 and 35, where  $S_{or}$  and  $S_{gr}$  refers to the residual  
 392 saturation of the oil and gas phase, respectively.  $k_{ro,max}$  and  $k_{rg,max}$  refer to the maximum relative  
 393 permeability of the oil and gas phase, respectively.  $n_o$  and  $n_g$  are two constants.

$$394 \quad k_{ro} = k_{ro,max} \left( \frac{S_o - S_{or}}{1 - S_{or} - S_{gr}} \right)^{n_o} \quad 34$$

$$395 \quad k_{rg} = k_{rg,max} \left( \frac{S_g - S_{gr}}{1 - S_{or} - S_{gr}} \right)^{n_g} \quad 35$$

396 The initial distribution of components of this case is shown in Table 5. The geomechanical  
 397 impact is not considered in this case. The input parameters, including the rock properties, are listed in  
 398 Table 6. We run this case with three different grid block sizes, namely 10 m\*10 m, 8 m\*8 m and 4 m\*4  
 399 m for 8 years. As the results, the oil pressure fields of the fracture system and the matrix rock at the  
 400 end of the production are shown in Figure 13. The comparison of the oil saturation fields of the matrix  
 401 rock system at the end of the first year of production and at the end of the eighth year of production is  
 402 shown in Figure 14. According to the results, the fractures in the vicinity of the hydraulic fracture get  
 403 quickly drained by the production, while the pressure inside the matrix rock system declines much  
 404 slower. As the pressure decreases, the gas phase expands and the oil saturation decreases.

405 We compare three types of initialization strategy of the flash calculation, namely initializing by  
 406 Wilson's equation, initializing by the primary variable from the previous NR iteration step, and initializing  
 407 by the DL preconditioner. In the second type, the initial guess of the equilibrium ration of the flash  
 408 calculation is calculated by the primary variable of the last Newton-Raphson iteration step of the same  
 409 grid block. In the second, the equilibrium ratio is obtained from the deep learning based proxy flash  
 410 calculation module. The comparison of the CPU time of the three types with different grid block sizes is  
 411 shown in Figure 15. According to Figure 15, the DL preconditioner effectively reduces the CPU time by  
 412 about 10% to 12%, compared to initializing by the equilibrium ratio from the previous iteration step. The  
 413 results presented in this case show that DL preconditioner is capable of accelerating the performance  
 414 of large scale compositional simulation for unconventional reservoirs.



415  
416 **Figure 12 Conceptual model of the case study with the DL based reservoir simulator.**

417  
418  
419 **Table 5 Initial distribution of components for deep learning based compositional reservoir**  
420 **simulation case.**

Component	Formula	Mole fraction
Methane	CH <sub>4</sub>	0.40
Ethane	C <sub>2</sub> H <sub>6</sub>	0.15
Propane	C <sub>3</sub> H <sub>8</sub>	0.15
Butane	C <sub>4</sub> H <sub>10</sub>	0.05
n-Pentane	C <sub>5</sub> H <sub>12</sub>	0.05
n-Heptane	C <sub>7</sub> H <sub>16</sub>	0.20

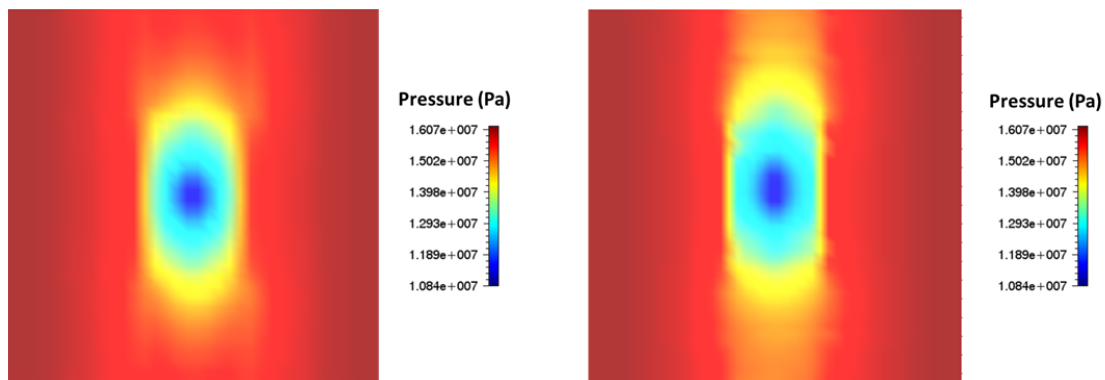
421  
422 **Table 6 Input parameters for fractured reservoir case.**

Property	Value	Unit
Permeability of the matrix rock	0.1	μd
Porosity of the matrix rock	0.01	dimensionless
Permeability of the hydraulic fracture	100	md
Porosity of the hydraulic fracture	0.2	dimensionless
Permeability of the fractures in SRV	50	md
Porosity of the fractures in SRV	0.1	dimensionless
Permeability of the fractures outside SRV	20	md

Porosity of the fractures outside SRV	0.05	dimensionless
Rock compressibility	0.0	dimensionless
Initial pressure	21.2	MPa
Initial temperature	120	°C
Production pressure	10.2	MPa
Pore radius	50	nm
Residual gas saturation ( $S_{gr}$ )	0.1	dimensionless
Residual oil saturation ( $S_{or}$ )	0.1	dimensionless
Maximum gas relative permeability ( $k_{rg,max}$ )	0.7	dimensionless
Maximum gas relative permeability ( $k_{ro,max}$ )	0.9	dimensionless
$n_g$	2.0	dimensionless
$n_o$	2.0	dimensionless

423

424



425

426

427

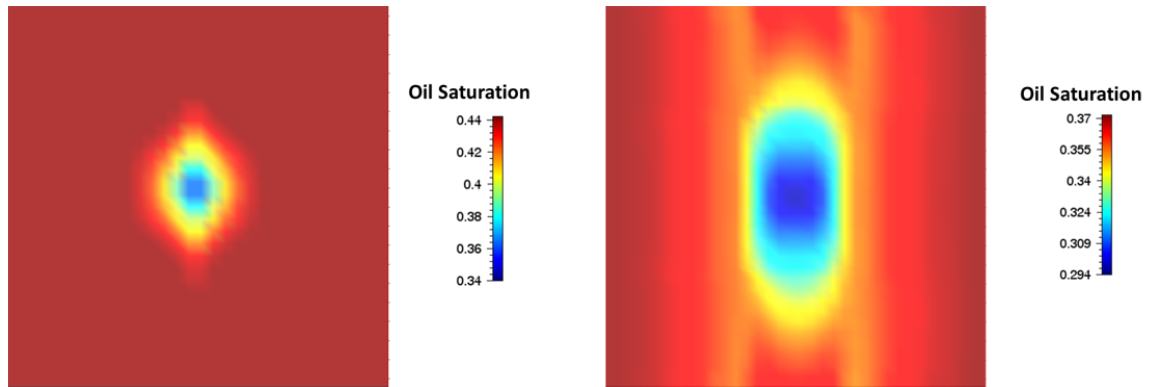
428

429

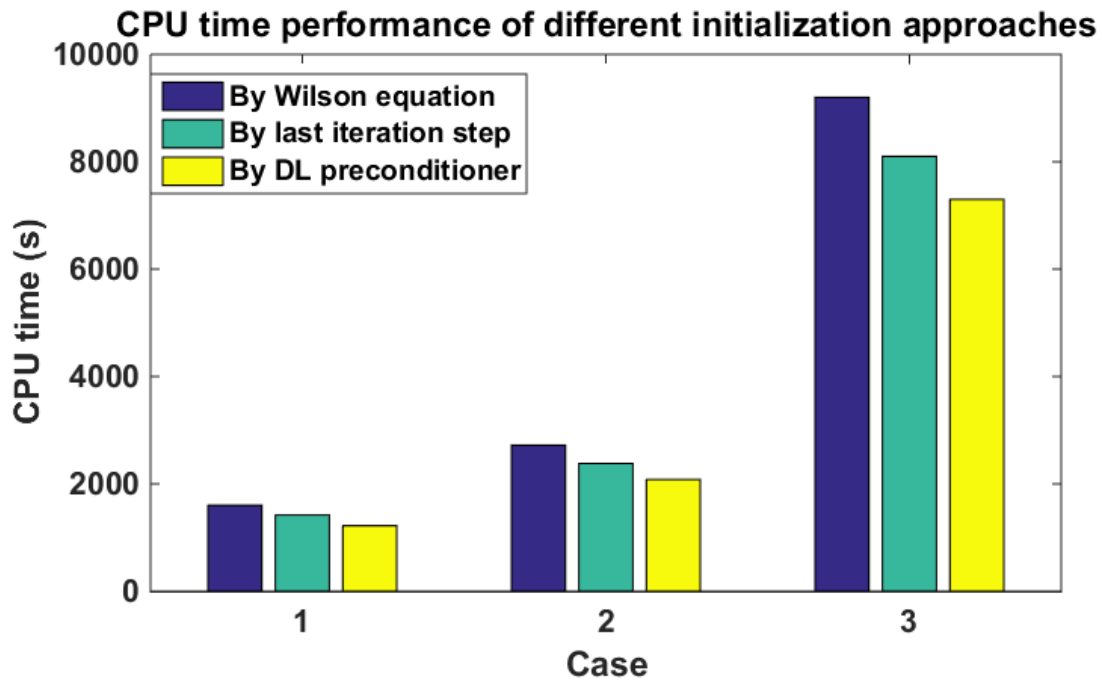
430

**Figure 13 Comparison of the oil pressure fields of the matrix rock system and the fracture system at the end of the 8-years production. Left: matrix rock system. Right: fracture system.**





431  
432 **Figure 14 Comparison of the oil saturation fields of the matrix rock system at the end of the first**  
433 **year of production and at the end of the eighth year of production. Left: end of the first year.**  
434 **Right: end of the eighth year.**  
435  
436



437  
438 **Figure 15 Comparison of the CPU time of the compositional reservoir simulation cases**  
439 **initialized with different initial guesses.**  
440  
441

## 442 6. Summary and Conclusion

443 To sum up, we have developed a data-based proxy flash calculator to speed up the time-  
444 consuming flash calculation. The proxy flash calculator adopts an initial guess obtained from the deep  
445 neural network, the accuracy of which is above 95%. With the implementation of the proxy calculator,  
446 the number of iterations of the flash calculation has been effectively reduced by about 50%. Moreover,  
447 the stability of the flash calculation has been improved by the DL based preconditioner, with the ratio of  
448 convergence increased from 90% to above 98% percent. This work is among the first trials in this area.

449 In the present work, the fully-connected neural network is used for the proxy flash calculator. In  
450 the future, other structures can also be tried and compared, for instance, the convolutional neural  
451 network and the recurrent neural network. Moreover, other portions of the simulator may also be  
452 accelerated by the deep learning techniques. For example, the wellbore flow part, which is a very time-  
453 consuming simulation of multiphase flow, can also be replaced by a DL based proxy calculator.

454

#### 455 **Acknowledgments**

456 The author would like to thank Energi Simulation for their kind support.

457

#### 458 **Reference**

- 459 [1] Jin B, Nasrabadi H. Phase behavior of multi-component hydrocarbon systems in nano-pores  
460 using gauge-GCMC molecular simulation. *Fluid Phase Equilib* 2016;425:324–34.  
461 doi:10.1016/J.FLUID.2016.06.018.
- 462 [2] Travalloni L, Castier M, Tavares FW. Phase equilibrium of fluids confined in porous media from  
463 an extended Peng–Robinson equation of state. *Fluid Phase Equilib* 2014;362:335–41.  
464 doi:10.1016/J.FLUID.2013.10.049.
- 465 [3] Xiong Y. Development of a compositional model fully coupled with geomechanics and its  
466 application to tight oil reservoir simulation. Colorado School of Mines. Arthur Lakes Library,  
467 2015.
- 468 [4] Zhang Y, Lashgari HR, Di Y, Sepehrnoori K. Capillary Pressure Effect on Hydrocarbon Phase  
469 Behavior in Unconventional Reservoirs. *SPE Low Perm Symp.*, Society of Petroleum Engineers;  
470 2016. doi:10.2118/180235-MS.
- 471 [5] Wang S, Pomerantz AE, Xu W, Lukyanov A, Kleinberg RL, Wu Y-S. The impact of kerogen  
472 properties on shale gas production: A reservoir simulation sensitivity analysis. *J Nat Gas Sci Eng*  
473 2017;48. doi:10.1016/j.jngse.2017.06.009.
- 474 [6] Kuila U, Prasad M. Understanding Pore-Structure And Permeability In Shales. *SPE Annu. Tech.*  
475 *Conf. Exhib.*, Society of Petroleum Engineers; 2011. doi:10.2118/146869-MS.
- 476 [7] Wang S, Lukyanov AA, Wang L, Wu Y-S, Pomerantz A, Xu W, et al. A non-empirical gas  
477 slippage model for low to moderate Knudsen numbers. *Phys Fluids* 2017;29.  
478 doi:10.1063/1.4974319.
- 479 [8] Wang S, Pan Z, Zhang J, Yang Z, Wang Y, Wu Y-S, et al. On the Klinkenberg effect of  
480 multicomponent gases. *Proc. - SPE Annu. Tech. Conf. Exhib.*, 2017.
- 481 [9] Wang S, Lukyanov AA, Wu Y-S. Second-order gas slippage model for the Klinkenberg effect of  
482 multicomponent gas at finite Knudsen numbers up to 1. *Fuel* 2019;235:1275–86.  
483 doi:10.1016/J.FUEL.2018.08.113.
- 484 [10] Okuno R, Johns R, Sepehrnoori K. A New Algorithm for Rachford-Rice for Multiphase

- 485 Compositional Simulation. SPE J 2010;15:313–25. doi:10.2118/117752-PA.
- 486 [11] Nichita DV, Gomez S, Luna E. Multiphase equilibria calculation by direct minimization of Gibbs  
487 free energy with a global optimization method. Comput Chem Eng 2002;26:1703–24.  
488 doi:10.1016/S0098-1354(02)00144-8.
- 489 [12] LeCun Y, Bengio Y, Hinton G. Deep learning. Nature 2015;521:436–44.  
490 doi:10.1038/nature14539.
- 491 [13] Gaganis V, Varotsis N. Machine Learning Methods to Speed up Compositional Reservoir  
492 Simulation. SPE Eur. Annu. Conf., Society of Petroleum Engineers; 2012. doi:10.2118/154505-  
493 MS.
- 494 [14] Gaganis V, Varotsis N. An integrated approach for rapid phase behavior calculations in  
495 compositional modeling. J Pet Sci Eng 2014;118:74–87. doi:10.1016/J.PETROL.2014.03.011.
- 496 [15] Kashinath A, Szulczewski ML, Dogru AH. A fast algorithm for calculating isothermal phase  
497 behavior using machine learning. Fluid Phase Equilib 2018;465:73–82.  
498 doi:10.1016/J.FLUID.2018.02.004.
- 499 [16] Tipping, E. M. The relevance vector machine. 12th Int. Conf. Neural Inf. Process. Syst., Denver,  
500 CO: MIT Press; 1999, p. 652–8.
- 501 [17] El-Sebakhy EA. Forecasting PVT properties of crude oil systems based on support vector  
502 machines modeling scheme. J Pet Sci Eng 2009;64:25–34. doi:10.1016/J.PETROL.2008.12.006.
- 503 [18] Rafiee-Taghanaki S, Arabloo M, Chamkalani A, Amani M, Zargari MH, Adelzadeh MR.  
504 Implementation of SVM framework to estimate PVT properties of reservoir oil. Fluid Phase  
505 Equilib 2013;346:25–32. doi:10.1016/J.FLUID.2013.02.012.
- 506 [19] Burges CJC. A Tutorial on Support Vector Machines for Pattern Recognition. Data Min Knowl  
507 Discov 1998;2:121–67. doi:10.1023/A:1009715923555.
- 508 [20] Kobayashi K, Komaki F. Information criteria for support vector machines. IEEE Trans Neural  
509 Networks 2006;17:571–7. doi:10.1109/TNN.2006.873276.
- 510 [21] Schölkopf B, Smola AJ. Learning with kernels : support vector machines, regularization,  
511 optimization, and beyond. 1st ed. MIT Press; 2002.
- 512 [22] Vapnik V. The Nature of Statistical Learning Theory. 2nd ed. New York: Springer; 2000.
- 513 [23] Gharbi RB., Adel M. Elsharkawy A, Karkoub M. Universal Neural-Network-Based Model for  
514 Estimating the PVT Properties of Crude Oil Systems 1999. doi:10.1021/EF980143V.
- 515 [24] Kamyab M, Sampaio JH., Qanbari F, Eustes AW. Using artificial neural networks to estimate the  
516 z-factor for natural hydrocarbon gases. J Pet Sci Eng 2010;73:248–57.  
517 doi:10.1016/J.PETROL.2010.07.006.
- 518 [25] Nikravesh M, Aminzadeh F, Zadeh LA. Soft computing and intelligent data analysis in oil  
519 exploration. Elsevier; 2003.
- 520 [26] Wang S. Numerical study of thermal-hydraulic-mechanical behavior of fractured geothermal

- reservoirs. Colorado School of Mines, 2015.
- [27] Wu Y. MSFLOW: Multiphase Subsurface Flow Model of Oil, Gas and Water in Porous and Fractured Media with Water Shutoff Capability, Documentation and User's Guide. Walnut Creek, California: 1998.
- [28] Narasimhan TN, Witherspoon PA. An integrated finite difference method for analyzing fluid flow in porous media. *Water Resour Res* 1976;12:57–64. doi:10.1029/WR012i001p00057.
- [29] Larsbo M, Roulier S, Stenemo F, Kasteel R, Jarvis N. An Improved Dual-Permeability Model of Water Flow and Solute Transport in the Vadose Zone. *Vadose Zo J* 2005;4:398. doi:10.2136/vzj2004.0137.
- [30] Wang S, Lukyanov AA, Wu;Yu-Shu. Application of algebraic smoothing aggregation two level preconditioner to multiphysics fluid flow simulations in porous media. *SPE Reserv. Simul. Conf.*, Galveston, Texas: 2019.
- [31] Wang L, Wang S, Zhang R, Wang C, Xiong Y, Zheng X, et al. Review of multi-scale and multi-physical simulation technologies for shale and tight gas reservoirs. *J Nat Gas Sci Eng* 2017;37:560–78. doi:10.1016/j.jngse.2016.11.051.
- [32] Wang L, Tian Y, Yu X, Wang C, Yao B, Wang S, et al. Advances in improved/enhanced oil recovery technologies for tight and shale reservoirs. *Fuel* 2017;210:425–45. doi:10.1016/J.FUEL.2017.08.095.
- [33] Macleod DB. On a relation between surface tension and density. *Trans Faraday Soc* 1923;19:38. doi:10.1039/tf9231900038.
- [34] Sugden S. VI.—The variation of surface tension with temperature and some related functions. *J Chem Soc, Trans* 1924;125:32–41. doi:10.1039/CT9242500032.
- [35] Sherafati M, Jessen K. Stability analysis for multicomponent mixtures including capillary pressure. *Fluid Phase Equilib* 2017;433:56–66. doi:10.1016/J.FLUID.2016.11.013.
- [36] Peng D-Y, Robinson DB. A new two-constant equation of state. *J Ind Eng Chem J Phys Chem Ind Eng Chem. Fundam J Agric Sci Van Stralen, S J O. Lnt J Heat Mass Transf I O* 1972;51:385–1082.
- [37] Lemmon, W. E. NIST Reference Fluid Thermodynamic and Transport Properties-REFPROP, Ver. 7.0. NIST Stand Ref Database 2002.
- [38] Michelsen ML. The isothermal flash problem. Part I. Stability. *Fluid Phase Equilib* 1982;9:1–19. doi:10.1016/0378-3812(82)85001-2.
- [39] Orbach O, Crowe CM. Convergence promotion in the simulation of chemical processes with recycle-the dominant eigenvalue method. *Can J Chem Eng* 1971;49:509–13. doi:10.1002/cjce.5450490414.
- [40] Reamer HH, Sage BH. Phase equilibria in hydrocarbon systems. Volumetric and phase behavior of the n-Decane-CO<sub>2</sub> System. *J Chem Eng Data* 1963;8:508–13. doi:10.1021/je60019a010.

- 557 [41] Iman RL, Iman, L. R. Latin Hypercube Sampling. *Encycl. Quant. Risk Anal. Assess.*, Chichester,  
558 UK: John Wiley & Sons, Ltd; 2008. doi:10.1002/9780470061596.risk0299.
- 559 [42] Stein M. Large sample properties of simulations using latin hypercube sampling. *Technometrics*  
560 1987;29:143–51. doi:10.1080/00401706.1987.10488205.
- 561 [43] Bottou L. Large-scale machine learning with stochastic gradient descent. *Proc.*  
562 *COMPSTAT'2010*, Heidelberg: Physica-Verlag HD; 2010, p. 177–86. doi:10.1007/978-3-7908-  
563 2604-3\_16.
- 564 [44] Chollet F. *Keras*. 2015.
- 565 [45] Bottou L. *Stochastic gradient descent tricks*, Springer, Berlin, Heidelberg; 2012, p. 421–36.  
566 doi:10.1007/978-3-642-35289-8\_25.
- 567 [46] Warren JE, Root PJ. The Behavior of Naturally Fractured Reservoirs. *Soc Pet Eng J*  
568 1963;3:245–55. doi:10.2118/426-PA.
- 569 [47] Gilman JR, Kazemi H. Improvements in Simulation of Naturally Fractured Reservoirs. *Soc Pet*  
570 *Eng J* 1983;23:695–707. doi:10.2118/10511-PA.
- 571 [48] Lim KT, Aziz K. Matrix-fracture transfer shape factors for dual-porosity simulators. *J Pet Sci Eng*  
572 1995;13:169–78. doi:10.1016/0920-4105(95)00010-F.
- 573 [49] Wu Y-S, Pruess K. A multiple-porosity method for simulation of naturally fractured petroleum  
574 reservoirs. *SPE Reserv Eng* 1988;3:327–36. doi:10.2118/15129-PA.
- 575 [50] Wu Y-S, Qin G. A generalized numerical approach for modeling multiphase flow and transport in  
576 fractured porous media. *Commun Comput Phys* 2009;6:85–108.
- 577 [51] Delshad M, Pope G. Comparison of the three-phase oil relative permeability models. *Transp*  
578 *Porous Media* 1989;4:59–83. doi:10.1007/BF00134742.
- 579

580

581 **Appendix A Parameters for flash calculation**

582

583

Table A.1 Parameters for the calculation of component properties

	<b>T<sub>c</sub> (K)</b>	<b>P<sub>c</sub> (MPa)</b>	<b>w</b>	<b>M<sub>w</sub> (g·mol<sup>-1</sup>)</b>	<b>a<sub>0</sub> (KJ·(kg·K)<sup>-1</sup>)</b>	<b>a<sub>1</sub> (KJ·(kg·K)<sup>-1</sup>)</b>
<b>CH<sub>4</sub></b>	190.56	4.599	0.0115	16.043	2.191	0.002672
<b>C<sub>2</sub>H<sub>6</sub></b>	305.32	4.872	0.0995	30.07	1.651	0.004384
<b>C<sub>3</sub>H<sub>8</sub></b>	369.83	4.248	0.1523	44.096	0.79	0.00468
<b>n-C<sub>4</sub>H<sub>10</sub></b>	408.14	3.648	0.2002	58.123	0.818	0.004255
<b>n-C<sub>5</sub>H<sub>12</sub></b>	469.7	3.37	0.2515	72.15	-0.218	0.001895

<b>n-C<sub>6</sub>H<sub>14</sub></b>	507.6	3.025	0.3013	86.177	-0.491	0.007187
<b>n-C<sub>7</sub>H<sub>16</sub></b>	540.2	2.74	0.3495	100.204	-0.756	0.007811
<b>n-C<sub>8</sub>H<sub>18</sub></b>	568.7	2.49	0.3996	114.231	-0.989	0.00836
<b>n-C<sub>9</sub>H<sub>20</sub></b>	594.6	2.29	0.4435	128.258	-1.236	0.008951
<b>n-C<sub>10</sub>H<sub>22</sub></b>	617.7	2.11	0.4923	142.285	-1.465	0.009484
<b>CO<sub>2</sub></b>	304.3	7.39	0.2236	44.01	0.727	0.003722

584

585

586

Table A. 2 Parachor values for all hydrocarbon components

<b>Component</b>	<b>Parachor</b>
CH <sub>4</sub>	77.0
C <sub>2</sub> H <sub>6</sub>	108.0
C <sub>3</sub> H <sub>8</sub>	150.3
n-C <sub>4</sub> H <sub>10</sub>	203.4
n-C <sub>5</sub> H <sub>12</sub>	231.5
n-C <sub>6</sub> H <sub>14</sub>	271.0
n-C <sub>7</sub> H <sub>16</sub>	312.5
n-C <sub>8</sub> H <sub>18</sub>	351.5
n-C <sub>9</sub> H <sub>20</sub>	393.0
n-C <sub>10</sub> H <sub>22</sub>	617.7

587